Bull. Mater. Sci., Vol. 36, No. 7, December 2013, pp. 1267–1274. © Indian Academy of Sciences.

Iron-substituted AB_5-type MH electrode

SUMITA SRIVASTAVA[a,*] **and R K UPADHYAYA**[b]
[a]Department of Physics, Government P.G. College, Uttarkashi 249 193, India
[b]Department of Physics, Government P.G. College, Rishikesh 249 201, India

MS received 10 November 2012; revised 3 March 2013

Abstract. **The present investigation is aimed to study $MmNi_5$-type (Mm = Mischmetal) hydrogen storage alloys with composition, $Mm_{0.8}La_{0.2}Ni_{3.7}Al_{0.38}Co_{0.3}Mn_{0.6-x}Mo_{0.02}Fe_x$ (x = 0, 0·1, 0·2 and 0·3). The alloys are synthesized by radio-frequency induction melting. To study their electrochemical properties via measurements of discharge capacity, activation process, rate capability and cyclic stability, electrodes are fabricated using as-synthesized and annealed version of the alloys. The maximum discharge capacity is recorded as 288 $mAhg^{-1}$ for the iron concentration, x = 0·1, as compared to 270 $mAhg^{-1}$ for the alloy electrode without iron. Similarly, 99% cyclic stability is observed in annealed alloy electrode (x = 0·1) as compared to 78% in the alloy electrode without iron. Hence, small amount of iron-substitution (x = 0·1) in the alloy is found to improve the electrochemical properties. This improvement is thought to be due to less pulverization of the alloy in electrochemically-cycled alloy, as confirmed through structural and microstructural characterizations carried out by X-ray diffraction phase analysis and scanning electron microscopy of as-fabricated and electrochemically-cycled electrodes.**

Keywords. **Metal hydride cell; iron substitution; electrochemical properties; structural characterization; pulverization characteristics.**

1. Introduction

One alloy type used in Ni–MH secondary cells is $MmNi_5$-type hydrogen storage material (Mm = Mischmetal). Many compositions typified by La/Mm(Ni–Al–Mn–Co)$_5$ use cobalt as an ingredient (Mishima *et al* 1993; Sakai *et al* 1994; Metzger *et al* 1998; Solonin *et al* 1999; Raju *et al* 2007; Zhao *et al* 2008; Anantha and Ananthi 2008; Anantha *et al* 2009; Fenga *et al* 2009; Liua *et al* 2009). Cobalt is an expensive metal and in a typical composition, $MmNi_{3.55}Mn_{0.4}Al_{0.3}Co_{0.75}$, it accounts for almost 50% of the total cost of the raw material (Li *et al* 2001). Hence, it is desirable to replace Co by a less expensive element without decreasing the hydrogen storage capacity significantly.

Keeping in view the fact that one of the criteria for increasing the hydrogen storage capacity is to bring a more electron-attracting element to the Ni site in the $MmNi_5$ alloy (Bououdina *et al* 2000). It has been found that because of the higher electron attracting power of Fe, when substituted in small concentration at the Ni site in the alloy, leads to enhancement of the hydrogen storage capacity (Pandey *et al* 2007; Singh *et al* 2007). Some studies on low-Co variants typified by $MmNi_{3.55}Mn_{0.4}Al_{0.3}Co_{0.75-x}Fe_x$ (x = 0·15, 0·55, 0·75) have been carried out by Moussa *et al* (2006, 2008). In these studies, maximum discharge capacity close to 266 $mAhg^{-1}$ has been obtained for the composition x = 0·15. The activation process has been completed in 16 cycles of charging–discharging to obtain the maximum discharge capacity. The discharge capacity and the number of charge–discharge cycles to activate the alloy have been found to decrease with increasing amount of Fe.

From the above discussion, it appears that Fe substitution at the Ni site in $MmNi_5$-type alloy improves its electrochemical properties, but this is not yet well established. The correlation between electrochemical and structural–microstructural characterizations has not been extensively explored for Fe-substituted material. The present study examines electrochemical properties of the new low-Co variant electrode material, $Mm_{0.8}La_{0.2}Ni_{3.7}Al_{0.38}Co_{0.3}Mn_{0.6-x}Mo_{0.02}Fe_x$ (x = 0, 0·1, 0·2 and 0·3). The correlation of electrochemical properties with structural and microstructural characteristics is also explored for this electrode material.

2. Experimental

2.1 *Synthesis of material and fabrication of negative electrode*

The intermetallic phases of $Mm_{0.8}La_{0.2}Ni_{3.7}Al_{0.38}Co_{0.3}Mn_{0.6-x}Mo_{0.02}Fe_x$ (x = 0, 0·1, 0·2 and 0·3) were prepared through solid state diffusion process by taking highly pure constituent elements of Mm (composition: La 22%, Ce 52%, Nd 15% and Pr 11%), La, Al, Co, Mn, Mo and Fe. To synthesize the alloy ingredients in a stoichiometric ratio were mixed, pelletized and then melted in a radio-frequency induction furnace under an argon atmosphere. The pellets

*Author for correspondence (sumita_uki1@rediffmail.com)

were remelted three times for the purpose of homogenization. A portion of as-synthesized alloy was annealed in flowing argon at a temperature of 1173 K for 20 h. To make the metal hydride (MH) electrode, powder consisting of particles $< 50\ \mu$m of as-synthesized or annealed alloy was selected. A mixture was prepared by taking the alloy, graphite powder and teflon suspension in a ratio of 85, 10 and 5 wt%. The resulting mixture was rolled against a smooth glass plate. This rolled sheet was folded around a nickel mesh of dimension: 2 × 2 cm and pressed at 6·4 × kg m^{-2} for 15 min. The physical thickness of this roll-compacted negative electrode was about 0·3 mm. Nickel–metal hydride (Ni–MH) electrochemical cell was formed by placing sintered nickel hydroxide electrodes on either side of a MH electrode in each cell, containing 6 M KOH electrolyte. The electrochemical capacity of the positive electrode ($Ni(OH)_2$) was designed to be sufficiently larger than that of the negative (MH) electrode. Both the negative and positive electrodes were inserted into the pockets made out of the polypropylene separator cloth. After preparing the Ni-MH cell, all electrochemical properties were monitored at 298 K. The negative electrode containing 0·5 g of hydrogen storage alloy was charged for 14 h and discharged to −0·6 V, with respect to Hg/HgO reference electrode at 28 mAg^{-1}. The potential of the negative electrode was monitored with an *x–y* recorder.

2.2 *Structural and microstructural characterization of MH electrode*

As-fabricated and electrochemically tested electrodes were subjected to X-ray diffraction characterization, employing a Philips X-ray diffractometer (PW 1710) equipped with a graphite monochromator that operated with CuKα radiation. The surface microstructures of MH electrodes were examined by means of a scanning electron microscope (SEM, Philips XL-20 series) that employed a 30 kV secondary electron imaging mode.

3. Results and discussion

3.1 *Structural and microstructural characterization*

The X-ray diffraction (XRD) profiles of as-fabricated and electrochemically-cycled electrodes using the alloy, $Mm_{0.8}La_{0.2}Ni_{3.7}Al_{0.38}Co_{0.3}Mn_{0.6-x}Mo_{0.02}Fe_x$ are shown in figures 1 and 2 corresponding to Fe concentrations $x = 0$ and 0·1, respectively. Similar XRD profiles are found for the alloys with $x = 0{\cdot}2$ and 0·3. The phase analysis through XRD patterns confirmed homogeneous composition and single phase hexagonal $CaCu_5$-type structure of symmetry *P6/mmm*. The lattice parameters and unit cell volumes of these alloys are given in table 1, in which an increase is noted in both the '*a*' and '*c*' parameters after substitution of Fe at the place of Ni in the parent alloy, $Mm_{0.8}La_{0.2}Ni_{3.7}Al_{0.38}Co_{0.3}Mn_{0.6-x}Mo_{0.02}Fe_x$ ($x = 0$). A continuous increase in the unit cell volume can be seen

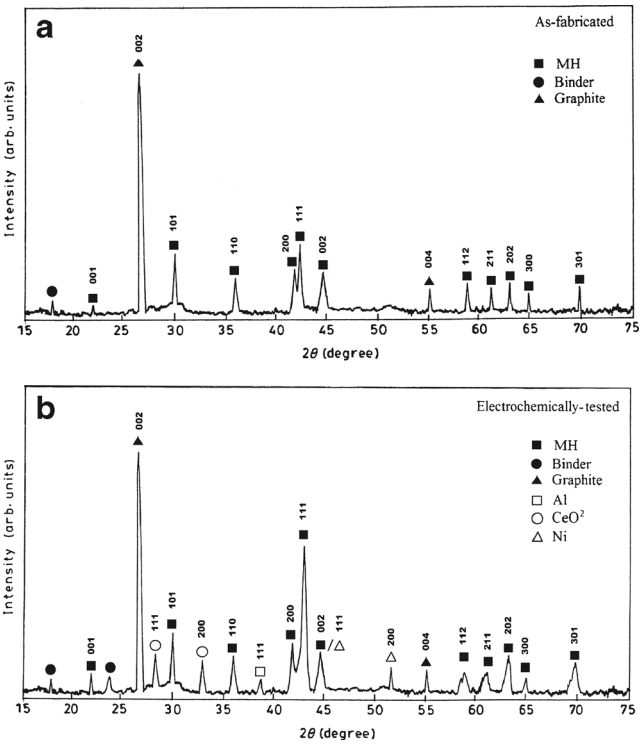

Figure 1. X-ray diffraction patterns of (**a**) as-fabricated and (**b**) electrochemically-cycled electrodes of $Mm_{0.8}La_{0.2}Ni_{3.7}Al_{0.38}Co_{0.3}Mn_{0.6-x}Mo_{0.02}Fe_x$ ($x = 0$); notice presence of XRD peaks corresponding to CeO_2, Al and Ni.

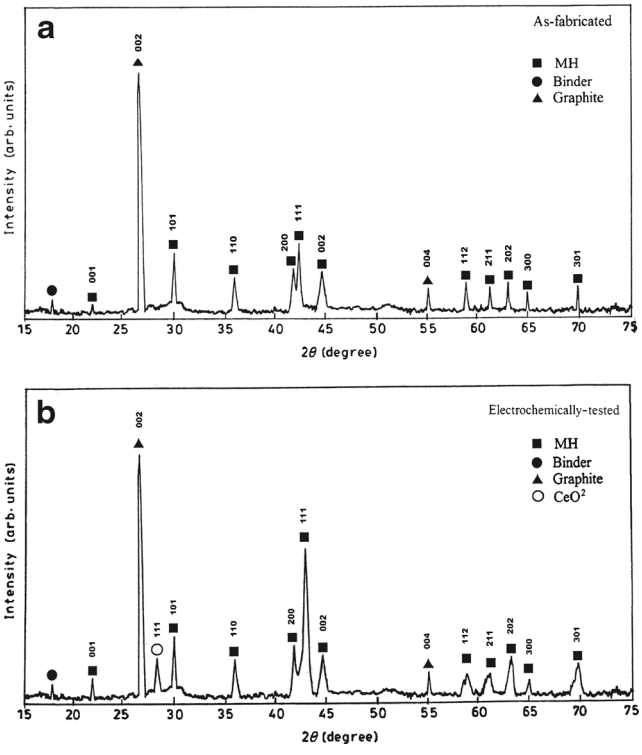

Figure 2. X-ray diffraction pattern of (**a**) as-fabricated and (**b**) electrochemically-tested electrodes of $Mm_{0.8}La_{0.2}Ni_{3.7}Al_{0.38}Co_{0.3}Mn_{0.6-x}Mo_{0.02}Fe_x$ ($x = 0{\cdot}1$); notice that XRD peak of CeO_2 alone is present.

Table 1. Lattice parameter and unit cell volume of as-fabricated and electrochemically-cycled $Mm_{0·8}La_{0·2}Ni_{3·7}Al_{0·38}Co_{0·3}Mn_{0·6-x}Mo_{0·02}Fe_x$ alloy electrodes.

	As-fabricated electrode			Electrochemically-cycled electrode			
	Lattice parameter		Unit cell volume	Lattice parameter		Unit cell volume	Change in unit cell volume,
Fe concentration (x)	a (Å)	c (Å)	V (Å^3)	a (Å)	c (Å)	V (Å^3)	ΔV (%)
0	5·0044	4·0644	88·1492	5·0390	4·0862	89·8517	1·931
0·1	5·0064	4·0660	88·2544	5·0068	4·0750	88·4639	0·237
0·2	5·0085	4·0693	88·4001	5·0088	4·0781	88·6019	0·228
0·3	5·0105	4·0712	88·5121	5·0108	4·0795	88·7031	0·216

with increasing concentration of Fe from $x = 0$ to 0·3 (figure 5). It may be due to large size of Fe atom (1·72 Å) in comparison with Ni atom (1·67 Å). Further, upon hydriding/electrochemical charging, when hydrogen atoms enter into the alloy lattice, they result in lattice expansion and thus increase in unit cell volume (Nasako *et al* 1998; Qin *et al* 2008). After the discharge process, a small increase in the unit cell volume (ΔV) is found in the alloy of the electrochemically-tested electrode as compared to the alloy of the as-fabricated electrode, due to residual hydrogen. Due to repeated charging–discharging cycle, the volume expansion leads to pulverization of the alloy. Hence, higher the volume expansion of the unit cell during hydriding/discharging of the alloy electrode, more pulverization of the alloy may take place. In the present investigation, the change in the unit cell volume in electrochemically-tested electrodes decreases continuously from 1·93 to 0·22% with increase in x from 0 to 0·3. While a measurable increase in the lattice parameter 'c' is observed, only a very small increase is observed in lattice parameter 'a' after electrochemical testing. It is due to larger volume expansion along the c-axis upon hydrogenation (Sakai *et al* 1994; Srivastava and Srivastava 1998). This volume expansion leads to the pulverization of the alloy after charge–discharge cycling. The analysis of variation in the lattice parameters and the unit cell volume in the electrochemically-cycled and as-synthesized alloys (table 1) reflects that the pulverization of the alloy decreases with increase in Fe concentration x in the alloy, $Mm_{0·8}La_{0·2}Ni_{3·7}Al_{0·38}Co_{0·3}Mn_{0·6-x}Mo_{0·02}Fe_x$. The large size of Fe atom which increases the size of unit cell volume may be the reason behind less expansion of unit cell upon hydriding–dehydriding/charging–discharging resulting in less pulverization of the alloy with higher Fe concentration. In the large unit cell, hydrogen atom may enter and come out easily from the interstitial sites giving less stress to the lattice and hence, less pulverization of the alloy.

Microstructural characterization of the as-synthesized and electrochemically-cycled alloys confirms less pulverization of the alloy with higher Fe concentration. Scanning electron micrographs of the as-synthesized and electrochemically cycled $Mm_{0·8}La_{0·2}Ni_{3·7}Al_{0·38}Co_{0·3}Mn_{0·6-x}Mo_{0·02}Fe_x$ alloy with $x = 0$ are shown in figure 3(a and b), respectively. Similarly, SEM micrographs of the as-synthesized and electrochemically-cycled $Mm_{0·8}La_{0·2}Ni_{3·7}Al_{0·38}Co_{0·3}Mn_{0·6-x}Mo_{0·02}Fe_x$ alloy with $x = 0·1$ are given in figure 4(a and b), respectively. A comparison of figures 3 and 4 reveals that surface morphology and particle size of the as-synthesized $Mm_{0·8}La_{0·2}Ni_{3·7}Al_{0·38}Co_{0·3}Mn_{0·6-x}Mo_{0·02}Fe_x$ alloys, with $x = 0$ (figure 3a) and $x = 0·1$ (figure 4a) are similar. However, the same for electrochemically-cycled $Mm_{0·8}La_{0·2}Ni_{3·7}Al_{0·38}Co_{0·3}Mn_{0·6-x}Mo_{0·02}Fe_x$ alloys with $x = 0$ (figure 3b) and $x = 0·1$ (figure 4b) are very different. The average particle size of the electrochemically-cycled $Mm_{0·8}La_{0·2}Ni_{3·7}Al_{0·38}Co_{0·3}Mn_{0·6-x}Mo_{0·02}Fe_x$ alloy is 2 and 5 μm for $x = 0$ and 0·1, respectively. The larger particle size in the alloy with higher Fe concentration suggests that lesser pulverization has taken place in this alloy after electrochemical cycling (figure 5).

The X-ray diffraction patterns in figures 1(a) and 2(a) indicate that as-fabricated electrodes of the alloy, $Mm_{0·8}La_{0·2}Ni_{3·7}Al_{0·38}Co_{0·3}Mn_{0·6-x}Mo_{0·02}Fe_x$ contain peaks of single phase MH, graphite and the binder. Whereas, the extra XRD peaks of CeO_2, Al and Ni can be noticed in XRD pattern of electrochemically-cycled alloy $Mm_{0·8}La_{0·2}Ni_{3·7}Al_{0·38}Co_{0·3}Mn_{0·6-x}Mo_{0·02}Fe_x$ ($x = 0$) (figure 1b). Only a small extra XRD peak of CeO_2 is present in the alloy, $Mm_{0·8}La_{0·2}Ni_{3·7}Al_{0·38}Co_{0·3}Mn_{0·6-x}Mo_{0·02}Fe_x$, ($x = 0·1$) (figure 2b) together with regular peaks of MH, graphite and the binder. The X-ray diffraction profile of the electrochemically-cycled electrode fabricated by the annealed version of the alloy, $Mm_{0·8}La_{0·2}Ni_{3·7}Al_{0·38}Co_{0·3}Mn_{0·6-x}Mo_{0·02}Fe_x$ ($x = 0·1$), is given in figure 6. No XRD peak corresponding to CeO_2 is visible in this XRD pattern. Thus, annealing of the alloy prevents the electrode material from oxidation during electrochemical charging–discharging. The lesser deterioration of the Fe-containing alloys may be due to their smaller extent of pulverization.

3.2 *Electrochemical studies*

3.2a *Activation process*: Activation is a process by which MH electrode attains maximum electrochemical capacity. When a MH electrode is charged for the first time, less hydrogen becomes available during discharging (Qin *et al* 2008). Repeated charging–discharging helps to achieve maximum electrochemical capacity. This is important for practical use in Ni–MH secondary cells. In the first charge–discharge cycle of the alloy

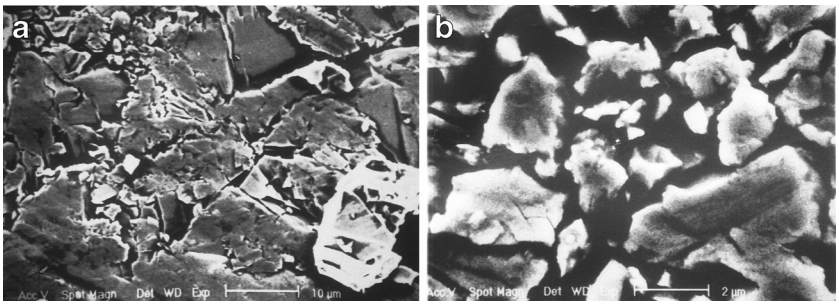

Figure 3. Scanning electron micrographs of (**a**) as-synthesized and (**b**) electrochemically cycled $Mm_{0·8}La_{0·2}Ni_{3·7}Al_{0·38}Co_{0·3}Mn_{0·6-x}Mo_{0·02}Fe_x$ alloy with $x = 0$.

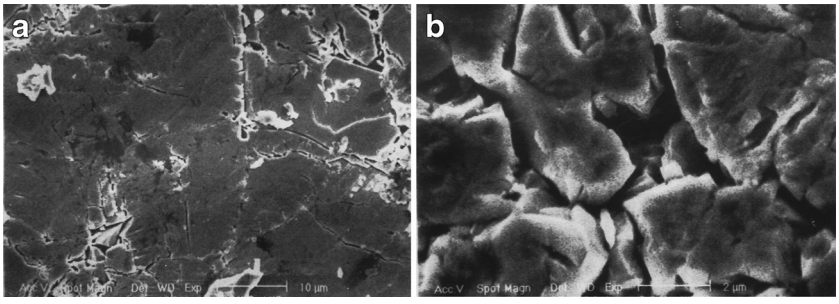

Figure 4. Scanning electron micrographs of (**a**) as-synthesized and (**b**) electrochemically-cycled $Mm_{0·8}La_{0·2}Ni_{3·7}Al_{0·38}Co_{0·3}Mn_{0·6-x}Mo_{0·02}Fe_x$ alloy with $x = 0·1$.

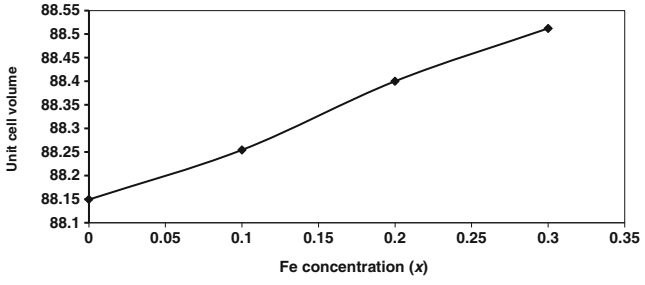

Figure 5. Variation in unit cell volume of as-synthesized $Mm_{0·8}La_{0·2}Ni_{3·7}Al_{0·38}Co_{0·3}Mn_{0·6-x}Mo_{0·02}Fe_x$ alloys with iron concentration 'x'.

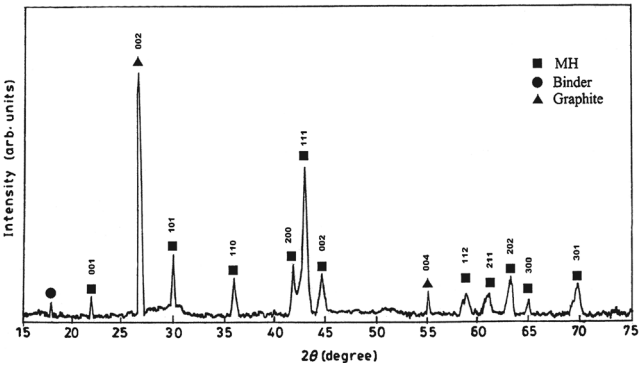

Figure 6. X-ray diffraction pattern of an electrochemically-cycled and annealed electrode with composition, $Mm_{0·8}La_{0·2}Ni_{3·7}Al_{0·38}Co_{0·3}Mn_{0·6-x}Mo_{0·02}Fe_x$, ($x = 0·1$). Note absence of CeO_2 XRD peak.

electrode, $Mm_{0·8}La_{0·2}Ni_{3·7}Al_{0·38}Co_{0·3}Mn_{0·6-x}Mo_{0·02}Fe_x$, the discharge capacity is 85% of the maximum value. The maximum discharge capacity of the alloy electrode $Mm_{0·8}La_{0·2}Ni_{3·7}Al_{0·38}Co_{0·3}Mn_{0·6-x}Mo_{0·02}Fe_x$ is obtained in the third, fifth, ninth and twelfth cycles corresponding to $x = 0$, 0·1, 0·2 and 0·3, respectively. It shows delayed activation of electrodes fabricated with alloys with a higher concentration of iron. This may be due to lower alloy pulverization with increasing Fe concentration, as is discussed in §3.1. During repeated charging–discharging of the electrode, the alloy material breaks into smaller particles due to pulverization, so fresh particle surfaces are thereby created, which lead to the increase of the reaction surface area and improvement of the electrode surface activation.

Earlier work (Nasako *et al* 1998; Moussa *et al* 2008) on the $MmNi_{3·553}Mn_{0·4}$ $Al_{0·3}Co_{0·6}Fe_{0·15}$ alloy report slow activation, as 16 cycles were required to activate the electrode completely. It may be mentioned that fast activation is a new finding in the present case. The annealing of the alloy improves the activation process significantly. In the case of the electrode prepared using an annealed alloy, a maximum capacity of 290 $mAhg^{-1}$ was achieved in the second electrochemical cycle. Such rapid activation may be due to the improved surface activity of annealed alloy electrodes.

3.2b *Discharge capacity*: The discharge capacity of the MH electrode, $Mm_{0·8}La_{0·2}Ni_{3·7}Al_{0·38}Co_{0·3}Mn_{0·6-x}Mo_{0·02}Fe_x$ is found to be 270, 288, 256 and 210 $mAhg^{-1}$ corresponding to $x = 0$, 0·1, 0·2 and 0·3, respectively. The discharge curves of MH electrode fabricated from $Mm_{0·8}La_{0·2}Ni_{3·7}Al_{0·38}Co_{0·3}Mn_{0·6-x}Mo_{0·02}Fe_x$ alloy corresponding to Fe concentration $x = 0$, 0·1, 0·2 and 0·3 are presented in figure 7. In this figure, four discharge curves are shown. The variation in the potential difference between negative and reference electrode (Hg/HgO) with hydrogen concentration (H/M) are normal throughout the discharging process. The open circuit voltage of MH electrode with respect to Hg/HgO electrode is 0·940, 0·928, 0·922 and 0·922 V corresponding to Fe concentration, $x = 0$, 0·1, 0·2 and 0·3, respectively. As observed, potential of the electrode shifts to a less negative value, due to the oxidation of desorbed hydrogen from the hydride. In each discharge curve, a continuous decrease in the potential is observed from an initial value of 0·930 to 0·900 V. Afterwards, a steep decrease in potential is noticed. The region exhibiting a voltage plateau between 0·930 and 0·900 V corresponds to the co-existence of α and β phases. The middle potential of the plateau region of the electrode is 0·926, 0·911, 0·910 and 0·909 V corresponding to $x = 0$, 0·1, 0·2 and 0·3. The voltage plateau value decreases with increase in the Fe concentration in the $Mm_{0·8}La_{0·2}Ni_{3·7}Al_{0·38}Co_{0·3}Mn_{0·6-x}Mo_{0·02}Fe_x$ alloy electrode.

It is observed that the substitution of Fe in the parent alloy, $Mm_{0·8}La_{0·2}Ni_{3·7}Al_{0·38}Co_{0·3}Mn_{0·6-x}Mo_{0·02}Fe_x$ ($x = 0$), by a small amount equal to $x = 0·1$ leads to an increase in discharge capacity from 270 to 288 $mAhg^{-1}$. A further increase of Fe concentration to $x = 0·2$ and 0·3 results in decrease of discharge capacity to 256 and 210 $mAhg^{-1}$, respectively. Increased discharge capacity because of Fe substitution ($x = 0·1$) is thought to be due to large size of Fe atom and higher electron attracting power of Fe ($3d^6$) against Ni ($3d^8$). However, upon increasing the Fe concentration at $x = 0·2$ and 0·3, a decrease in the discharge capacity and activation is noticed. This decrease may be due to segregation of Fe. In the present investigation, XRD does not confirm the formation of iron oxide in the alloy electrode after several charging–discharging cycles. This may be due to small amount of iron oxide in the present case. However, earlier study (Ayari *et al* 2005) confirms the segregation of Fe, as it is very much prone to oxidation. Hence, Fe when substituted in small concentration leads to enhancement of the hydrogen storage capacity due to its higher electron attracting power.

3.2c *Discharge rate capability*: To study the dependence of discharge capacity on discharge rate, the discharge current was varied from 28 to 140 mAg^{-1}. The variation of discharge capacity with discharge current of the $Mm_{0·8}La_{0·2}Ni_{3·7}Al_{0·38}Co_{0·3}Mn_{0·6-x}Mo_{0·02}Fe_x$ electrodes is illustrated in figure 8. On increasing the discharge current from 28 to 84 mAg^{-1}, all the electrodes exhibit a loss in their normal capacity by nearly 10%. On further increase in discharge current from 84 to 140 mAg^{-1}, a significant loss is observed in the normal discharge capacity of the electrodes. The loss in discharge capacity of the electrodes is found to be 32, 20, 22 and 22% corresponding to $x = 0$, 0·1, 0·2 and 0·3, respectively. Hence, the discharge rate capability is improved by the substitution of Fe in the parent alloy.

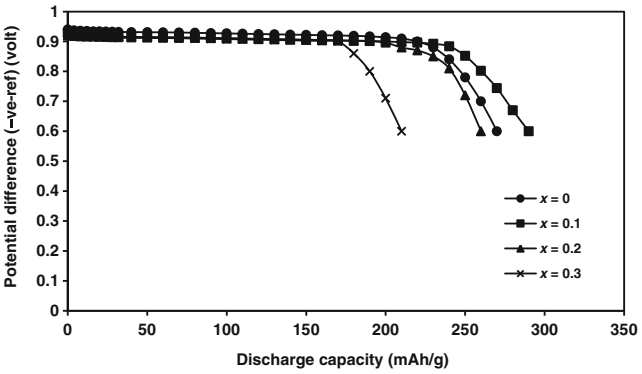

Figure 7. Discharging curves of $Mm_{0·8}La_{0·2}Ni_{3·7}Al_{0·38}Co_{0·3}Mn_{0·6-x}Mo_{0·02}Fe_x$ electrodes with $x = 0$, 0·1, 0·2 and 0·3.

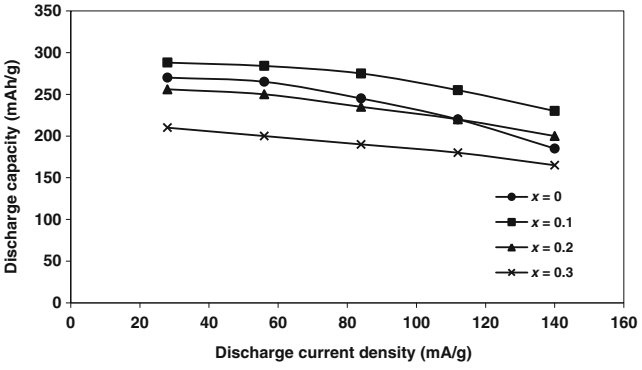

Figure 8. Discharge capacity *vs* discharge current density of $Mm_{0·8}La_{0·2}Ni_{3·7}Al_{0·38}Co_{0·3}Mn_{0·6-x}Mo_{0·02}Fe_x$ alloy electrodes with $x = 0$, 0·1, 0·2 and 0·3.

The discharge rate capability of the negative electrode in the Ni–MH cell is mainly determined by the mass-transfer process in the bulk MH alloy powder and the charge-transfer process at the interface between the MH alloy powder and the electrolyte. Hence, it appears that Fe substitution improves one or both processes to facilitate higher discharge rate capability. Due to a large unit cell volume in Fe-substituted alloy, hydrogen atoms can move easily to interstitial positions. Wei *et al* (2007) report a higher value of diffusion coefficient in the alloy containing Fe. The fast diffusion of hydrogen atoms enhances the mass transfer process in the electrode. However, pulverization of the alloy particles in the electrode during charge–discharge results in poor electronic connection between particles. The reduced pulverization of the Fe-substituted alloy in the present case may reduce this effect. The lesser oxidation of the observed Fe alloy may increase electrochemical activity of the electrode.

Thus Fe-substitution in the alloy appears to enhance the charge-transfer process; hence the combined effect of faster mass and charge transfer is being responsible for improved discharge rate capability.

3.2d *Cyclic performance*: The short-term cyclic performance of the family of $Mm_{0·8}La_{0·2}Ni_{3·7}Al_{0·38}Co_{0·3}Mn_{0·6-x}Mo_{0·02}Fe_x$ alloy electrodes showing variation in discharge capacity as a function of cycle number is illustrated in figure 9. It shows a residual capacity of 78, 87, 94 and 95% of the maximum discharge capacity after 20 charge–discharge cycles. A similar test on the electrode fabricated with an annealed $Mm_{0·8}La_{0·2}Ni_{3·7}Al_{0·38}Co_{0·3}Mn_{0·6-x}Mo_{0·02}Fe_x$ alloy with $x = 0·1$, shows 99% residual capacity after the same number of cycles (figure 10). These results reveal improved cyclic stability of the electrodes with increase in Fe concentration. The cyclic performance is significantly improved by employing the annealed alloy in the electrode.

The fundamental reasons for the capacity decay of the alloy electrodes are oxidation and pulverization of the alloy during the charge–discharge cycle (Xu *et al* 2007). The pulverized alloy creates a new surface which is oxidized when it comes into contact with the alkaline electrolyte solution. The oxide or hydroxide layer acts as a barrier to hydrogen diffusion and leads to a decrease in the number of hydrogen atoms, which can be absorbed by the material. Pan *et al* (1999) and Geng *et al* (1999) assume that the loss in discharge capacity results from the deterioration of the negative electrode material with an increase in the number of charge–discharge cycles. In fact, during cycling, rare-earth elements such as, La and Ce segregate to the grain boundaries, where they are subjected to corrosion. This results in an increase in the electronic resistance between alloy grains, which in turn decreases the electrode discharge capacity.

Furthermore, disintegration resulting from pulverization leads to a further decrease in electronic conductivity and thus decreases the cycle life. Thus, cycle stability of the alloy mainly depends on the anti-pulverization capability of the alloy. The structural characteristic parameters given in table 1 show that the change in the unit cell volume after electrochemical testing decreases continuously from 1·93 to 0·22% with increase in Fe concentration from $x = 0$ to $x = 0·3$. This suggests that less pulverization takes place after repeated charging–discharging in the $Mm_{0·8}La_{0·2}Ni_{3·7}Al_{0·38}Co_{0·3}Mn_{0·6-x}Mo_{0·02}Fe_x$ electrode because of its increase in Fe concentration. Microstructural evaluations using SEM also confirm this. This may be the reason for the improved cyclic performance of the electrode having a higher concentration of Fe as shown in figure 9.

On the other hand, the formation of CeO_2 (as-confirmed by XRD profile of figures 1(b) and 2(b) after repeated cycles of charging–discharging may be the reason for the deterioration of the electrode material in the present investigation. The absence of CeO_2 peak in the XRD profile of the annealed $Mm_{0·8}La_{0·2}Ni_{3·7}Al_{0·38}Co_{0·3}Mn_{0·6-x}Mo_{0·02}Fe_x$ electrode with $x = 0·1$ (figure 6), is due to the alloy composition which becomes more homogeneous at 1173 K.

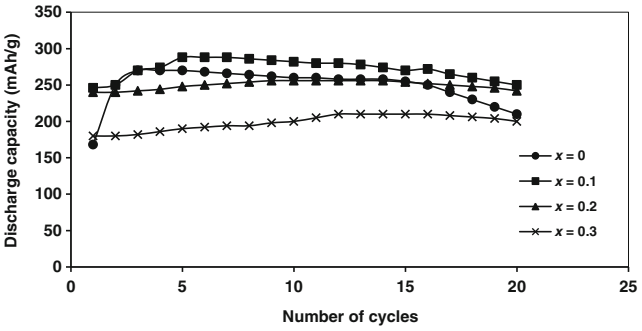

Figure 9. Cycle performance of $Mm_{0·8}La_{0·2}Ni_{3·7}Al_{0·38}Co_{0·3}Mn_{0·6-x}Mo_{0·02}Fe_x$ alloy electrodes with $x = 0$, 0·1, 0·2 and 0·3.

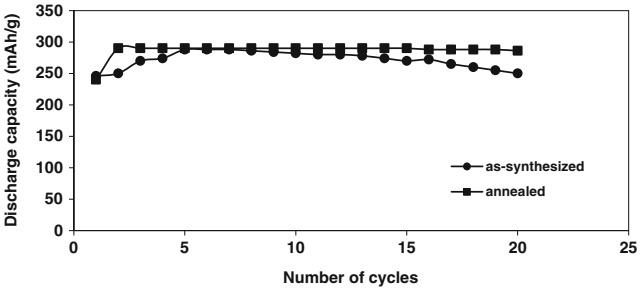

Figure 10. Cycle performance of as-synthesized and annealed $Mm_{0·8}La_{0·2}Ni_{3·7}Al_{0·38}Co_{0·3}Mn_{0·6-x}Mo_{0·02}Fe_x$ electrodes with $x = 0·1$.

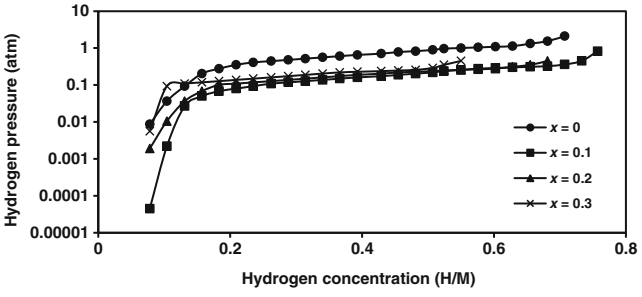

Figure 11. PCT curves of $Mm_{0·8}La_{0·2}Ni_{3·7}Al_{0·38}Co_{0·3}Mn_{0·6-x}Mo_{0·02}Fe_x$ alloy with $x = 0$, 0·1, 0·2 and 0·3, calculated from figure 7 discharge curves using Nernst equation.

3.2e *Pressure-composition isotherm (PCT)*: In the present investigation, pressure-composition isotherms (PCT) were obtained from the electrochemical composition isotherm (ECT) using the Nernst equation. This is due to low (sub-atmospheric) plateau pressure of hydride materials used as Ni–MH cell anodes which lie below atmospheric pressure. Direct PCT isotherm, therefore, requires specially-designed high vacuum equipment resulting in difficult experiments.

Wang *et al* (1997) presented a simplified Nernst equation for the specific parameters of the Ni–MH cell. At 298 K this equation is given by:

$$E = -0·93045 - 0·029547 \log PH_2, \quad (1)$$

Table 2. Discharge capacity, absorbed hydrogen concentration and desorption plateau pressure of $Mm_{0·8}La_{0·2}Ni_{3·7}Al_{0·38}Co_{0·3}Mn_{0·6-x}Mo_{0·02}Fe_x$ alloy electrodes.

Fe concentration (x)	Discharge capacity (mAh/g)	Hydrogen concentration (wt%)	Hydrogen concentration (H/M)	Plateau pressure (atm)
0	270	1·01	0·70	0·707
0·1	288	1·07	0·75	0·174
0·2	256	0·95	0·66	0·188
0·3	210	0·78	0·54	0·204

where E is the potential difference in volts between negative MH electrode and a Hg/HgO reference electrode and PH_2 the corresponding hydrogen pressure in atm units. Following (1), PCT curves were determined for $Mm_{0·8}La_{0·2}Ni_{3·7}Al_{0·38}Co_{0·3}Mn_{0·6-x}Mo_{0·02}Fe_x$ alloy electrodes with $x = 0$, 0·1, 0·2 and 0·3, using the discharge curves shown in figure 7. PCT curves show variation in hydrogen equilibrium pressure with respect to hydrogen concentration and are presented in figure 11. PCT curves can be divided into three parts. The first part, localized below the H/M = 0·15, corresponds to the solid solution α-phase. The second part, localized between H/M = 0·15 and 0·65, corresponds to the co-existence of two phases α and β, where β is the hydride phase. Finally, the third part, localized beyond H/M = 0·65, corresponds to the β-phase, where the entire alloy is transformed into the hydride phase. The desorption PCT curves given in figure 11 show a decrease in the plateau pressure of the parent alloy, when Fe is substituted in small amounts ($x = 0·1$). However, a slight increase in the plateau pressure is obtained upon increasing the Fe concentration 'x' in the $Mm_{0·8}La_{0·2}Ni_{3·7}Al_{0·38}Co_{0·3}Mn_{0·6-x}Mo_{0·02}Fe_x$ alloy. The value of hydrogen storage capacity, discharge capacity and plateau pressure of the $Mm_{0·8}La_{0·2}Ni_{3·7}Al_{0·38}Co_{0·3}Mn_{0·6-x}Mo_{0·02}Fe_x$ alloy electrodes are given in table 2. The plateau pressure is evaluated at the mid-point of the plateau region between H/M = 0·15 and 0·65.

In the present study, equilibrium hydrogen pressure of all the alloy electrodes corresponding to the plateau of the curves are below 1 atm. These values indicate that all the hydrides of $Mm_{0·8}La_{0·2}Ni_{3·7}Al_{0·38}Co_{0·3}Mn_{0·6-x}Mo_{0·02}Fe_x$ are stable at room temperature and can be used as negative electrodes. The low-pressure plateau indicates a low inner pressure of the Ni-MH battery, which is beneficial in terms of safety, especially for electric tools and electric vehicle batteries (Mishima *et al* 1993).

4. Conclusions

The alloys, $Mm_{0·8}La_{0·2}Ni_{3·7}Al_{0·38}Co_{0·3}Mn_{0·6-x}Mo_{0·02}Fe_x$ ($x = 0$, 0·1, 0·2 and 0·3), have been synthesized by a radio-frequency induction melting method. Structural analysis confirms a hexagonal $CaCu_5$-type crystal lattice for the alloys. Analysis of X-ray diffraction profiles show less oxidation of the electrode fabricated by the alloy with iron, after repeated charging–discharging cycles. The evaluations of lattice parameters and SEM micrographs confirm less pulverization of the electrode with higher concentration of iron in the alloy. The substitution of iron in small amount in the parent alloy improves all the electrochemical properties. Further increase in the iron concentration favours some properties like higher discharge rate-capability and cycle life. On the other hand, few electrochemical properties become poor, like activation process and discharge capacity.

The number of activation cycles to achieve maximum discharge capacity is 3, 5, 9 and 12, corresponding to iron concentrations, $x = 0$, 0·1, 0·2 and 0·3. The discharge capacity of the $Mm_{0·8}La_{0·2}Ni_{3·7}Al_{0·38}Co_{0·3}Mn_{0·6-x}Mo_{0·02}Fe_x$ electrodes are 270, 288, 256 and 210 $mAhg^{-1}$ for $x = 0$, 0·1, 0·2 and 0·3, respectively. The cyclic stability is improved to 78, 87, 94 and 95% of the maximum discharge capacity as the iron concentration, x increased in the range of 0, 0·1, 0·2 and 0·3, respectively after 20 cycles. Annealing of the alloy improves cyclic stability (99% *vs* 87% after 20 cycles) of the electrode. This improvement is thought to be due to less oxidation and lower pulverization of the hydride material of the electrode after repeated cycling. In conclusion, it can be said that iron substitution in the alloy can improve its electrochemical characteristics when substituted in small amounts.

Acknowledgements

The authors are grateful to Prof. O N Srivastava Banaras Hindu University, Varanasi, for helpful discussion.

References

Anantha M V and Ananthi P 2008 *Int. J. Hydrogen Energy* **33** 5779

Anantha M V, Ganesana M, Renganathana N G and Lakshmi S 2009 *Int. J. Hydrogen Energy* **34** 356

Ayari M, Boncour V P, Lamloumi J, Guegan A P and Guillot M 2005 *J. Magn. Magn. Mater.* **288** 374

Bououdina M, Soubeyroux J L, Rango D P and Fruchart D 2000 *Int. J. Hydrogen Energy* **25** 1059

Fenga H, Liua X, Tiana X, Chia B, Huanga L H and Xub J 2009 *Int. J. Hydrogen Energy* **34** 1886

Geng M, Han J W, Feng F and Northwood D O 1999 *J. Electrochem. Soc.* **146** 2371

Li C J, Wang F R, Cheng W H, Li W and Zhoo W T 2001 *J. Alloys Compds* **315** 218

Liua X, Fenga H, Tiana X, Chia B, Yana S and Xub J 2009 *Int. J. Hydrogen Energy* **34** 7291

Metzger W, Westfall R and Hermann A 1998 *Int. J. Hydrogen Energy* **23** 1179

Mishima R, Miyamura H, Sakai T, Kuriyama N, Ishikawa H and Uchara I 1993 *J. Alloys Compds* **192** 176

Moussa B M, Abdellaoui M, Mathlouthi H, Lamloumi J and Percheron Guegan A 2006 *J. Alloys Compds* **407** 256

Moussa B M, Abdellaoui M, Mathlouthi H, Lamloumi J and Percheron Guegan A 2008 *J. Alloys Compds* **458** 410

Nasako K, Ito Y and Hiro N 1998 *Int. J. Hydrogen Energy* **23** 921

Pan H, Ma J, Wang C, Chen S, Wang X, Chen C and Wang Q 1999 *J. Alloys. Compds* **293–295** 648

Pandey S K, Srivastava A and Srivastava O N 2007 *Int. J. Hydrogen Energy* **32** 2461

Qin F, Guo L H, Chen J P and Chen Z J 2008 *Int. J. Hydrogen Energy* **33** 709

Raju M, Manimaran K, Ananth M V and Renganathan N G 2007 *Int. J. Hydrogen Energy* **32** 1721

Sakai T, Miyamura H, Kuriyama N, Ishikawa H and Uchara I 1994 *Zeit. Fur. Phys. Chem. Bd 183 S* **333–346** 1373

Singh R K, Lototsky M V and Srivastava O N 2007 *Int. J. Hydrogen Energy* **32** 2971

Solonin Y M, Skorokhod V V, Solonin S M, Kolomiets L L, Savin V V and Bratanich T I 1999 *Int. J. Hydrogen Energy* **24** 277

Srivastava S and Srivastava O N 1998 *Int. J. Hydrogen Energy* **23** 7

Wang C S, Wang X H, Lei Y Q, Chen C P and Wang Q D 1997 *Int. J. Hydrogen Energy* **22** 1117

Wei X, Liu S, Dong H, Zhang P, Liu Y, Zhu J and Yu G 2007 *Electrochim. Acta* **52** 2423

Xu Y, Chen C, Wang X and Wang Q 2007 *Int. J. Hydrogen Energy* **32** 537

Zhao X, Ding Y, Yang M and Ma L 2008 *Int. J. Hydrogen Energy* **33** 81